Communications Earth & Environment https://doi.org/10.1038/s43247-026-03302-8

Article in Press

Estimating tectonic coastal uplift requires accounting for sea-level variations caused by rapid sediment redistribution

Received: 11 March 2025

Accepted: 5 February 2026

Cite this article as: Ho, A., Shyu, J.B., Tan, E. *et al.* Estimating tectonic coastal uplift requires accounting for sea-level variations caused by rapid sediment redistribution. *Commun Earth Environ* (2026). https://doi.org/10.1038/s43247-026-03302-8

Andrew Ho, J. Bruce H. Shyu, Eh Tan & Ken L. Ferrier

Estimating tectonic coastal uplift requires accounting for sea-level variations caused by rapid sediment redistribution

Andrew Ho[1], J. Bruce H. Shyu[1]*, Eh Tan[2], Ken L. Ferrier[3]

[1]Department of Geosciences, National Taiwan University, Taipei, Taiwan

[2]Institute of Earth Sciences, Academia Sinica, Taipei, Taiwan

[3]Department of Geoscience, University of Wisconsin-Madison, Madison, Wisconsin, USA

*Corresponding author: jbhs@ntu.edu.tw

Abstract

Information about past sea-level change is crucial for understanding coastal tectonic movements and seismic hazards. Locally, sediment isostatic adjustment (SIA) induced by erosional unloading and depositional loading could play an important role on sea-level change. However, such effects are commonly neglected, potentially leading to biased estimates of vertical tectonic deformation rate. Here we constructed a new sediment transfer history for Taiwan, where erosion and deposition are among the fastest on Earth, and used it to drive the numerical sea-level model to quantify SIA effects on the sea-level change and tectonic uplift estimates. Our simulations revealed that SIA could cause substantial spatial variation in sea-level change along Taiwan's coasts, producing local relative sea-level change of >200 meters since 122 ka. We found that neglecting SIA effects can result in overestimation and underestimation of tectonic coastal uplift rates by up to 90% or more. Our results highlight the global importance of considering spatially varying SIA-driven sea-level changes when using paleo-sea-level indicators to characterize coastal tectonic movements.

Introduction

Relative sea-level histories have been widely used to quantify coastal deformation rates [1, 2], which are the fundamental parameters for characterizing tectonic movements, understanding the geometry of active faults, and assessing seismic hazards. Traditionally, studies on coastal uplift far from major ice sheets use a global mean sea-level curve or curves constructed locally by dated paleo-sea-level records from areas that have undergone similar glacial isostatic adjustment (GIA) effects [1, 3, 4]. For example, paleo-sea-level data since 4.5 ka from Penghu Island [5] and older data from Singapore [6] or the Sunda Shelf [7] have often been utilized to reconstruct the sea-level curve

since the Last Glacial Maximum (LGM) for Taiwan's coasts [8, 9]. The curve is then compared with ages and elevations of uplifted paleo-sea-level indicators along the coast to evaluate vertical tectonic movements.

However, locally, sea level may be substantially affected by sediment isostatic adjustment (SIA) due to different erosional and depositional patterns, which perturbs crustal elevation and the Earth's gravitational field [10, 11]. In areas subjected to erosion, the unloading causes crustal uplift, inducing relative sea-level fall. Conversely, in depositional areas, additional loading from sediments causes crustal subsidence, leading to relative sea-level rise (**Fig. 1a**). This dynamic creates spatially varying patterns of sea-level change and records, and thus affects estimates of coastal tectonic uplift contributed by coseismic and interseismic deformation of active faults, which provide insights to potential seismic activity. For instance, if a coast has experienced uplift due to erosion nearby, the total observed crustal uplift would not be entirely driven by tectonics, but rather would be the sum of a component driven by tectonics and a component driven by erosional unloading (SIA). In other words, the actual tectonic uplift would be overestimated if SIA effects were not accounted for (**Fig. 1b** Case A). In contrast, in areas where sediment deposition has driven crustal subsidence, the actual tectonic uplift would be underestimated if SIA effects were neglected (**Fig. 1b** Case B). Therefore, in regions with rapid erosion and deposition, calculating tectonic uplift rates by using a mean sea-level curve, without considering local SIA effects, is likely to result in inaccurate estimates of tectonic uplift and seismic risks.

The effects of SIA on sea-level should be particularly substantial in regions with rapid sediment redistribution, such as Taiwan. The island and its surrounding offshore areas are subject to some of the fastest erosion and deposition on Earth [12, 13, 14] due to the combined effect of high precipitation under a sub-tropical climate and rapid crustal deformation rates [15, 16] that result from the ongoing collision between Eurasian and Philippine Sea plates [17] (**Supplementary Notes 1**). This presents a great opportunity to explore SIA effects in an active orogenic belt (**Fig. 2a**). In addition, the ongoing orogeny gives rise to numerous active faults [18, 19], which deform coastlines and pose severe seismic hazards. This makes accurately estimating coastal tectonic uplift rates crucial and urgent for understanding these seismogenic structures.

In this study, we quantitatively analyzed how rapid erosion and deposition would affect sea level and its records during the last glacial-interglacial cycle (122-0 ka) along the coasts of Taiwan. This time interval encompasses the period with most well-preserved and dated paleo-sea-level indicators in Taiwan (e.g., ref [8, 20, 21]) and provides a representative timescale for capturing variations in sediment transfer during sea-level fluctuations and the associated SIA effects. We

then used the resulting modeled spatial and temporal variations in sea level to calculate revised estimates of tectonic uplift rates along each coast of Taiwan. Quantifying such SIA effects is complicated since it requires a broad understanding of sediment redistribution histories, ice-sheet loading changes, Earth rheology, shoreline migration, change of gravitational fields and rotation axis, and the complex interactions between these factors. This can be overcome by using gravitationally self-consistent sea-level models that take these components into account [10, 22, 23]. This approach was recently applied to Taiwan [24], which suggested that SIA responses to sediment redistribution may have been large around Taiwan, based on sea-level simulations driven by an applied sediment redistribution history generated with a relatively small set of empirical constraints. Here we build on this work by constructing a new time-varying sediment transfer history for Taiwan with substantially higher spatial and temporal resolution, larger spatial coverage, and the incorporation of more precise and extensive erosion and deposition rates. We then use this reconstruction to model sea-level responses to sediment redistribution and a global ice loading history [25] on spherically symmetric Earth models (**Methods**).

Sediment transfer history reconstruction

Computing rates and patterns of SIA requires driving the sea-level model with a detailed sediment transfer history, which describes where and how much sediment have been eroded and deposited, and determines how SIA process would proceed. To build a comprehensive and detailed sediment transfer history for Taiwan, we compiled more than 1000 published erosion and deposition rate measurements from over 100 studies over a range of spatial and temporal scales (**Supplementary Notes 2**).

To construct an erosion rate map, we used denudation rates derived from cosmogenic nuclides [13, 26, 27] and detrital zircon fission-tracks [26], and exhumation rates calculated from fully reset apatite fission track (AFT) ages [28, 29] with a geothermal gradient map [30] (**Supplementary Notes 2.2**; **Fig. 2c, d**). Despite the different timescales represented by these different methods, erosion rates derived from all these studies display a good agreement [13, 26], and the spatial distribution of erosion rates aligns with topographic relief, slope and steepness, showing a strong tectonic control. For example, on the eastern flank of the Central Mountain Range, erosion rates are generally higher and increase northward. Not only is this pattern consistent with steeper channel slopes and higher relief there, and the northward maturation of collision of the Taiwan orogen, but it also matches the higher and northward-increasing metamorphic grades of exposed rocks. On the western side, lower rates in the central area corresponds to the lower topographic relief near the Puli Basin (**Fig.**

2a, c, d). Temporally, since tectonic conditions did not have major change in the past 122 kyr, we apply temporally steady erosion rates under the assumption that the tectonic drivers of erosion have remained consistent during studied period. In addition, previous work has shown that patterns of these erosion rates are decoupled from precipitation patterns [13]. Thus, although some studies suggest that precipitation may be lower during glacial periods compared to the Holocene [31, 32, 33], it is unlikely that glacial-interglacial climate fluctuations drastically altered long-term denudation rate patterns.

To generate deposition rate maps at different time, we compiled age data from both onshore and offshore sediment cores [34, 35, 36] (**Supplementary Notes 2.3 and 2.4**) and isopach maps derived from submarine seismic profiles [14, 37] (**Fig 2c, d**). To account for temporal variations in deposition rate driven by the temporal fluctuations in sea level during the glacial-interglacial cycle, we designed a time-varying deposition model. We first identified two events that mark major changes in deposition rates according to sediment records since the LGM: the sequence boundary of post-LGM sediments on the coastal plains that marks the onset of rapid deposition at ~15 ka [38, 39], and the inundation of the Taiwan Strait and the continental shelf at ~14 ka. The post-LGM period can therefore be divided into three periods with different depositional patterns (**Fig. 2b**). During the sea-level highstand of 14-0 ka, sediment was deposited parallel to Taiwan's northwestern coast in the Taiwan Strait due to along-current transport [14, 40], and rapid subaerial sedimentation occurred on coastal plains [39] (**Fig. 2c**). During the transition stage of 15-14 ka, when the sea surface was lower and the Taiwan Strait was exposed, sediment bypassed this region, so we restricted sediment deposition to the deeper southwestern offshore and northeastern Okinawa Trough [41]. During the lowstand prior to 15 ka, core records indicate that deposition on the coastal plains was much slower than that during the highstand and more sediment was transferred to the two deeper offshore areas (**Fig. 2d**). Finally, since there are fewer deposition rate constraints before LGM, we used a simulated sea-level curve driven by global ice volume change to extrapolate the earlier deposition scenarios before LGM by assuming a similar pattern of deposition when the sea-level height was the same (**Fig. 2b**). The deposition rates and patterns of highstand and transition we applied to 14-0 ka and 15-14 ka, respectively, are thus assigned to 122-72 ka and 72-70 ka, respectively. With this sediment transfer history of Taiwan, extremely rapid sediment redistribution within this small region can be clearly noted, with local erosion and deposition rates as high as 7 and 18 mm yr-1, respectively.

Sea-level modeling results

Using these erosion and deposition rate maps representing the sediment transfer history, we modeled the spatial and temporal changes in sea-surface equipotential (ΔG) and crustal elevation (ΔR) in response to the sediment redistribution (SIA) and global ice volume variation since 122 ka (**Fig. 3 c, f and b, e**), which reflects the gravitational and deformational perturbation, respectively. For locations with negligible changes in grounded ice thickness or sediment thickness, like the coasts of Taiwan that preserved paleo-sea-level indicators, changes in sea-level (ΔSL_{GR}) are obtained by taking the difference of the two (**Fig. 3 a, d**; **Methods**):

$$\Delta SL_{GR} = \Delta G - \Delta R \quad (1)$$

This reflects that under a mostly stable ΔG, SIA-driven uplift (positive ΔR) causes relative sea-level fall (negative ΔSL_{GR}) and vice versa (**Methods**).

We conducted simulations using two spherically symmetric Earth models, which both have elasticity and density parameters taken from PREM [42] and viscosity profiles based on ref. [24]. The only difference between these Earth models is in their effective elastic lithosphere thickness (LT), one with LT = 10 km and one with LT = 30 km. We denote these as the LT10 and LT30 simulations, respectively (**Fig. 3 a–c and d–f**). The LT10 condition corresponds to southwestern and eastern Taiwan [43, 44, 45], with an ocean-continent transition or oceanic crust beneath, and the LT30 condition corresponds to the northern part of the coastal plain and areas west of Taiwan that are on continental crust [46, 47]. These two values represent the lower and upper bounds of LT around Taiwan.

Our modeling results illustrate extreme spatial variation in cumulative sea-level change (ΔSL_{GR}) and crustal deformation (ΔR) around Taiwan since 122 ka (**Fig. 3a, b, d, e**). The patterns and magnitudes of the two fields are similar, showing that ΔR (i.e., crustal uplift and subsidence due to SIA) is the dominant contributor to ΔSL_{GR} in our simulations. The cumulative change in the sea-surface equipotential (ΔG), by comparison, is much smaller (**Fig. 3c, f**), consistent with previous studies of sea-level responses to sediment redistribution [11]. In addition, despite the difference in wavelength and amplitude of modeled ΔSL_{GR} in LT10 and LT30 simulations, we found that coastlines near the eroding mountains, such as in eastern and northeastern Taiwan, have indeed experienced crustal uplift due to SIA, leading to relative sea-level fall in both results. Conversely, coasts near depositional basins, like Penghu and the southwestern coast, have undergone SIA-driven subsidence, resulting in relative sea-level rise (**Fig. 3a, b, d, e**). Furthermore, the Taitung coast in eastern Taiwan and Liuchiu Island off the southwestern coast exhibit distinctly different SIA effects, despite being less than 100 kilometers apart (**Fig. 3a**), marking an intriguing case with opposite crustal responses of coasts within such a short distance.

Quantitatively, our simulations indicate that SIA may produce sea-level changes of tens to

hundreds of meters over 100-kyr timescales along Taiwan's coasts (**Fig. 3a, d**). This is far greater than the 6-8 meters of change in global mean sea level (GMSL) attributed to ice volume fluctuations and global GIA since the Last Interglacial [48, 49] (**Fig. 4**). The largest SIA-driven uplift and subsidence and the related sea-level changes of coasts occurred along the central eastern coast and Liuchiu Island, where the LT is close to 10 km. There, we found exceptionally large changes in sea-level of over 200 and 70 meters, respectively, since the Last Interglacial (**Fig. 3a**). In comparison with other regions worldwide with reported substantial SIA effects, Taiwan has undergone much larger SIA-driven sea-level change (**Table 1**). For example, it has been shown that SIA may drive crustal subsidence and sea-level rise of up to ~15 m along the coast of Indus Delta [11] and up to ~10 m at east Texas coast [50] since the Last Interglacial, both of which are substantially smaller than the SIA-driven subsidence at Liuchiu Island. Likewise, SIA-induced uplift of up to ~50 m has been documented along the southern coast of Norway over one glacial-interglacial cycle [51], which is less than one-fourth of the amount we found along Taiwan's central eastern coast. The large amplitude, short wavelength variations in sea level in Taiwan are the results of the extremely rapid sediment redistribution and the relatively thin elastic lithosphere.

From the modeled relative sea-level (RSL) histories at each coast (**Fig. 3g-l**), it is also clear that SIA drives strong spatial variations in sea-level change. For instance, **Fig. 3i** shows accounting for SIA increases at the central eastern coast, while **Fig. 3l** shows accounting for SIA decreases RSL at Hengchun. The magnitude of sea-level change due to SIA also varies between coasts. This illustrates the importance of using different sea-level curves for different places—even sites that are relatively close together—in regions like Taiwan with remarkably rapid and spatially varying erosion and deposition.

The modeled curves also show that SIA effects accumulate over time as materials are continuously eroded and deposited, causing modeled sea-level curves that account for SIA to diverge progressively more over time from modeled sea-level curves that neglect SIA (**Fig. 3g-l**). This suggests that older paleo-sea-level markers would be affected more than younger ones, resulting in greater errors in estimates of tectonic uplift. In summary, our results point out that SIA has substantial impacts on sea-level change histories.

Comparing modeled and observed sea-level histories

To validate our simulations, we compared our modeled sea-level curves that account for SIA to dated paleo-sea-level markers in areas where tectonic movement is relatively small (tectonically stable) (**Fig. 5a-c**). One such area is the northeastern coast of Taiwan, where tectonic uplift was

proposed to have stopped in the past million years [52]. Despite this, previous studies have found mid-Holocene marine terraces that are higher than the proposed paleo-sea level at that time [53], suggesting recent coastal uplift. Our modeled sea-level curves can fit the dated marine terrace records only when SIA effect is considered (**Fig. 5b**), indicating that SIA is the dominant driver of coastal uplift here. Likewise, at Penghu, stable since the late Miocene [54], our modeled sea-level curves with SIA are slightly closer to the dated mid-Holocene records than those without SIA (**Fig. 5c**). These comparisons show that simulations taking SIA into account yield modeled RSL histories that fit measured RSL histories better.

Implications of re-estimation of tectonic uplift for seismic hazard assessment

Finally, we utilized our modeled sea-level curves that account for SIA to re-estimate the tectonic uplift at each coast in tectonically active areas of Taiwan (**Fig. 5d-h**; **Methods**; **Supplementary Notes 3**). At coasts subjected to uplift due to isostatic responses, tectonic uplift would be overestimated if SIA were neglected. For example, dated Marine Isotope Stage (MIS)-5c marine terraces along the northwestern coast with an elevation of 90 meters were previously thought to represent a tectonic uplift of 128 meters using a sea-level curve that neglects SIA [55]. However, in our LT30 simulations, SIA-driven rock uplift since MIS-5c was as high as 73 m, implying that the actual tectonically-driven component of uplift may be only 55 meters, less than half of the previous estimate (**Fig. 5d**). Correcting for SIA in this manner lowers the inferred tectonic uplift rate from 1.27 ± 0.09 mm yr-1 to 0.55 ± 0.04 mm yr-1 (**Fig. 5h**) and lowers the corresponding inferred slip rate of the active Miaoli frontal structure [19], which in turn results in a longer inferred average earthquake recurrence interval (**Supplementary Notes 4.1**). Similar overestimates of tectonic uplift are observed along the eastern coast (**Fig. 5e**), where SIA also drives rock uplift. Our simulations suggest that estimates of tectonic uplift rates in this area may need to be lowered by around 1–2 mm yr-1, representing a 10–90% decrease from previous estimates (**Fig. 5h, Supplementary Table S13 in Supplementary Data 1**).

In contrast, in areas that have subsided due to rapid deposition, estimates of tectonic uplift are likely to be underestimated. Take Liuchiu Island for example (**Fig. 5f**), where our modeled sea-level curves from the LT10 simulation with and without SIA effects differ from one another by 7 m at 7 ka (mid-Holocene). This means one would overlook 7 meters of tectonic uplift if one were to neglect SIA when using mid-Holocene marine terraces to calculate tectonic uplift, equivalent to an underestimate of 107%. We thus propose the tectonic uplift rate at this site should be revised from 0.96 ± 0.14 to 1.98 ± 0.28 mm yr-1 (**Fig. 5h, Supplementary Notes 4.2 and Table S13 in**

Supplementary Data 1). Furthermore, the underestimate of tectonic contribution introduced by neglecting SIA becomes even greater when using the older MIS-5a terrace in the same area. In our simulation, sediment loading caused MIS-5a sea-level markers to subside by 64 meters from 80 ka to the present, which, if neglected, would cause a 147% underestimate of tectonic uplift rate (**Fig. 5f**). In other words, the actual uplift contributed by the East Liuchiu Island structure beneath Liuchiu Island may be more than twice of what was previously thought, posing higher seismic risks for southwestern Taiwan. Such underestimates can also be noticed at Hengchun at the southern tip of Taiwan, but to a much smaller extent since the effects of erosional unloading and depositional loading counteract each other in this area (**Fig. 5g**).

Moreover, these SIA effects have more implications for neotectonic interpretation of coastal features. For example, some marine terraces with regular age and elevation intervals have been interpreted as formed by co-seismic uplift of large earthquakes (e.g., ref. [8]). However, if the coast has been affected by substantial isostatic responses, the uplift history may be more complex than that suggested by the terraces. Additionally, coastal tectonic uplift rates have often been used to constrain the subsurface geometry of active faults (e.g., ref. [56]). Re-examination of such rates with SIA effects would also influence our knowledge of the general shape of fault systems. Therefore, accounting for SIA is also crucial for understanding tectonic processes and geological history in coastal regions.

Uncertainties in sea-level modeling and future prospects

Uncertainties in simulating sea-level responses to changes in surface loading lie in several aspects related to three model inputs: the chosen Earth model, the reconstructed sediment redistribution history, and, though less important in this study, the global ice history.

In this study, we used spherically symmetric Earth models to explore SIA effects on sea-level changes for Taiwan. Such models are adept at capturing many aspects of sea-level responses to surface loading (e.g., ref. [23]), but they are unable to account for lateral heterogeneity in lithospheric thickness and mantle viscosity, such as those documented beneath Taiwan (e.g., ref. [57]). Prior studies have successfully simulated sea-level responses on Earth models with three-dimensional variations in the mantle and lithosphere (e.g., ref. [58, 59]), but such models are far more computationally expensive than those on spherically symmetric Earth models (e.g., ref. [59, 60, 61]), and applying them to our study area would require first developing a 3D Earth model that incorporates high-resolution variations in Earth structure around Taiwan. Such an approach is

beyond the scope of this study, but we highlight that this would be a potentially productive direction for future work.

Given these limitations, it is challenging to quantitatively assess the effect of lateral variations in Earth structure on SIA. Nonetheless, certain effects can be anticipated qualitatively. For example, local lithospheric weakening along plate-boundary faults could largely amplify subsidence due to sediment loading [62].This effect may be particularly important in southwestern Taiwan, where rapid sedimentation occurs near the plate boundary and the lithospheric flexure has been shown to be much larger than other areas in Taiwan [43]. In such cases, tectonic uplift could be underestimated even more if SIA-induced subsidence were neglected. On the other hand, the presence of asthenosphere with lower viscosity may expedite short-term elastic responses while attenuating viscous responses over longer timescales. Undoubtedly, future improvements will depend on the development of high-resolution 3-D Earth structure models for Taiwan and advances in computational ability.

The sediment transfer history developed in this study also carries uncertainties, primarily due to the uneven spatial distribution of rate measurements and the scarcity of constraints further back in time. For instance, there are far more dated cores on the coastal plains than in offshore regions, and the constraints on deposition rates before LGM are particularly sparse. However, our reconstruction has integrated nearly all existing erosion and deposition rate data, and sensitivity test results indicate that the sea-level predictions are insensitive to depositional scenario during sea-level fluctuations of MIS 5. Future refinements on the sediment transfer history may focus on improving the data completeness, such as more dated offshore cores and basin-averaged erosion rates.

Concluding Remarks

Based on our findings, it is still apparent that SIA effects arising from erosion and deposition are capable of substantially changing local relative sea level with extreme spatial variability, which would cause great errors in the estimation of tectonic movements. This observation is applicable to other regions worldwide with rapid sediment transfer. In particular, active orogenic belts usually have higher erosion and sedimentation rates [63, 64] and thinner elastic lithosphere [65, 66], both of which would enhance the effects of SIA. An accurate assessment of tectonic activities is also crucial for improving constraints on seismic hazards in these regions. Although erosion and deposition rates in some orogens may not be as high as in Taiwan and would have slower SIA processes, sea-level markers older than MIS-5e may still be preserved under such conditions. Since the effects of SIA

becomes more pronounced through time, large errors would still result from using these markers to calculate tectonically driven changes in crustal elevation, both for regions experiencing uplift as well as those experiencing subsidence, where the SIA-induced uplift would lead to underestimation in tectonic subsidence if SIA effect is neglected. In summary, our results highlight the global importance of considering sea-level fluctuations resulting from sediment redistribution when using paleo-sea-level markers to understand coastal tectonic movements and landscape evolution.

Methods

Sea-level modeling

We used the gravitationally self-consistent sea-level model of ref. [10] to compute sea-level changes in response to changes in surface loading by ice mass variations and erosion and deposition of sediment. This model accounts for feedbacks of Earth rotational effects, shoreline migration, and sediment loading, and neglects variations in sediment compaction and water storage [67]. The model requires three inputs: a sediment transfer history that quantifies spatial and temporal changes in sediment loads, an ice history that quantifies spatial and temporal changes in grounded ice thickness, and an Earth model that determines solid Earth responses to these surface mass loading changes. The model uses these inputs to compute the resulting gravitational, deformational, and rotational perturbations, which in turn are used to calculate sea-level changes by solving the sea-level equation.

The sea-level equation that defines the change in sea-level from one time to another is written as

$$\Delta SL = \Delta G - (\Delta R + \Delta H + \Delta I) \quad (2)$$

where ΔH and ΔI are the change in sediment and grounded ice thickness, respectively, which are the known inputs to drive the model, while ΔG and ΔR are the responding changes in sea-surface equipotential (geoid) and bedrock elevation, respectively. Each term in Equation 2 is defined at every point on Earth's surface and is a function of time. The sea-level field is thus also globally defined, both on land and over oceanic regions. This is the same as the geologically defined relative sea-level, which considers local sea-surface relative to ground surface, and is thus useful in interpreting geological records.

In this study, the sea-level equation is solved by first calculating the total loading change of the oceans, ice, and sediments by the equation

$$\Delta L = \rho_W \Delta S + \rho_I \Delta I + \rho_H \Delta H \quad (3)$$

where ρ_W, ρ_I, ρ_H denote, in turn, the density of sea water, ice, and sediment, and ΔS is the change in ocean thickness, where S is only non-zero over the oceans. Next, the responses of ΔG and ΔR to the total change in loading ΔL are computed using the viscoelastic Love number theory [68]. Finally, we calculated ΔSL by combining the four fields through equation (2).

Next, we define several important parameters used in the text, including relative sea-level (RSL) and ΔSL_{GR}. The RSL at a certain time is defined as the sealevel of any past time t with respect to present day t_p and can be directly obtained by the time series of ΔSL as follows

$$RSL(t) = \Delta SL(t) - \Delta SL(t_p) = -\Delta SL(\text{from } t \text{ to } t_p) \quad (4)$$

In the equation, RSL predicts the elevation of a paleo-sea-level marker with age t when not deformed by tectonics.

In the analysis of sea level changes in this paper, we used a modified definition following ref. [11, 69] that excludes the contributions to ΔSL from direct topographic changes due to erosion or deposition (ΔH) and ice thickness change (ΔI). Specifically, we can write ΔSL_{GR} defined in equation (1) and the relative sea-level as

$$RSL_{GR}(t) = \Delta SL_{GR}(t) - \Delta SL_{GR}(t_p) \quad (5)$$

ΔSL_{GR} is an accurate measure of sea-level change for paleo-sea-level markers for two reasons. First, for regions like Taiwan without ice-sheet cover, there is no change in ice thickness locally ($\Delta I = 0$). Second, and more importantly, since most of the sea-level indicators we used, such as shoreline angles of marine terraces or sediments on the terrace, are benchmarked to bedrock height R and are deformed together with the crust, these markers also ignore the direct height change from sediment thickness variation above them. Therefore, as long as the distance between marker and bedrock remains constant through time, which means the compaction beneath the sea-level marker is negligible, the sea-level change relative to the marker would be the same as that relative to the bedrock. The dated RSL records should thus be compared to RSL_{GR} (or ΔSL_{GR}) that is dependent only on sea-surface and bedrock height change (ΔG and ΔR). Hence, our discussion focuses on sea-levels of ΔSL_{GR} and RSL_{GR}.

Input models

Among the three inputs of the sea-level model in our study, the sediment transfer history ΔH was built by compiling numerous data of erosion and deposition rates as mentioned in the text. More details and constraints about constructing this sediment model is elaborated in the **Supplementary Notes 2**.

The ΔI history used in our simulation is from the global ICE-6G_C model [25, 70]. This new version of the model follows the ICE-5G model [71], and is refined by fitting extensive vertical land motion data from GNSS measurements and verified by comparing predicted gravitational field changes to the gravity data from the GRACE satellite. The model describes the ice thickness changes of the major ice sheets of the world, including the Laurentide, Cordilleran, and Innuitian ice sheet complex of North America, the Fennoscandian and Barents Sea ice complexes in Northwestern Eurasia, as well as Greenland and Antarctica. ICE-6G is characterized by the Last Glacial Maximum (LGM) at 26 ka, followed by the deglaciation phase, which ended at around 4-5 ka, with two melt water pulses at approximately 14 and 11 ka resulting in more rapid global mean

sea-level rise. The ice history was extended back to the Last Interglacial (122 ka) following the GMSL curve based on benthic $\delta^{18}O$ records by ref. [72] (e.g., ref. [73]).

The Earth models adopted in this study are of a spherically symmetric Maxwell viscoelastic Earth, with radially varying rheological properties. The elasticity and density profiles are based on the preliminary reference Earth model (PREM) [42]. The Earth models are characterized by a layer of purely elastic lithosphere with a specified thickness (LT) and two layers of viscoelastic mantle. The upper and lower mantle are separated by the seismic discontinuity at the depth of 660 kilometers, with viscosities of 5×10^{20} Pa s and 5×10^{21} Pa s, respectively (e.g., ref. [24, 74]). To mimic the elastic lithosphere thickness around Taiwan, we prescribed two LT values of 10 and 30 km, which are consistent with the lowest and highest LT in the region [43, 44, 45, 46, 47]. These values are distinctly lower than those used in the global GIA models, such as the 90 km used in VM2 and VM5a Earth model [25, 70, 71], illustrating the thinner elastic lithosphere in young orogenic belts [65, 66]. To capture the short-wavelength spatial variability of sediment load and the resulting sea-level changes, we performed simulations at the higher spherical harmonic degree and order 1024.

Coastal uplift rates calculation

Uplift rates (UR) of each coast of Taiwan were calculated from the amount of deformation recorded by selected sea-level markers divided by its dated or inferred age (T). The deformation amount (ΔR_{tec}) is determined by subtracting the depositional paleodepth (d), and paleo-sea-level elevation (RSL_{GR}) derived from the sea-level curves we modeled, from the sample elevation (H).

$$UR = \frac{(H - d - RSL_{GR})}{T} \tag{6}$$

Since not all of the samples formed at mean sea level, the correction term d, which accounts for depositional paleodepth and is determined by the type of sample, its occurrence, or its depositional environment, is needed. This ensures that $(H - d)$ represents the current elevation of dated paleo-mean sea level. The $(H - d)$ term can also be referred to as RSL_{GR_marker} or $-\Delta SL_{GR\_marker}$. In most cases, the samples are close to the bedrock or shoreline angle and their elevations thus represent the heights of paleo-sea-level, giving $d = 0$ for these samples. However, some samples on the eastern coasts were collected from thick marine sediments in the absence of observable bedrock risers. In such cases, we interpret the parameter d based on identified sedimentary facies. For example, ref. [8] identified samples in well-sorted, parallel laminated or low angle cross-bedded sands as being deposited in foreshore zone, with $-1 < d < 1$ m. More details about the sedimentary facies and depositional paleodepth of each sample can be found in the

Supplementary Table S13 in Supplementary Data 1.

For each sample, we calculated tectonic uplift rates before and after considering SIA effects by comparing with modeled sea-level curves with and without consideration of SIA at each coast (as shown in **Fig. 5d-g**). The revised tectonic uplifts accounting for SIA for well-preserved sea-level markers (i.e., where $\Delta H = 0$) can be calculated by setting the total rock uplift (ΔR_{ob}) as the sum of tectonically-driven rock uplift (ΔR_{tec}) and SIA-driven rock uplift (ΔR_{SIA}) [24, 48]. With this, we can write the sea-level change recorded by those sea-level markers as $\Delta SL_{GR\_marker} = \Delta G - (\Delta R_{tec} + \Delta R_{SIA})$, and rearrange it as $\Delta R_{tec} = \Delta G - \Delta R_{SIA} - \Delta SL_{GR\_marker} = RSL_{GR\_marker} - RSL_{GR\_SIA}$, where RSL_{GR_SIA} is the relative sea level accounting for SIA.

We then took the difference between the calculated rates and normalized it to the rate without accounting for SIA (which are approximately the rates calculated in previous studies) to estimate the correction percentage of tectonic uplift rates.

Data Availability

The datasets used in this study are available on Zenodo (https://doi.org/10.5281/zenodo.18212597). This repository contains Excel files comprising the compiled rates of sediment redistribution used to reconstruct the sediment transfer history, as well as the information of paleo-sea-level indicators used to evaluate tectonic coastal uplift rates. Due to the large size of Supplementary Tables S1–9 and S13, these tables are provided as separate tabs in the Excel file of Supplementary Data 1.

Code Availability

The gravitationally self-consistent sea-level model can be accessed at https://github.com/jaustermann/SLcode.

References

1. Grant LB, Mueller KJ, Gath EM, Cheng H, Edwards RL, Munro R*, et al.* Late Quaternary uplift and earthquake potential of the San Joaquin Hills, southern Los Angeles basin, California. *Geology* 1999, **27**(11)**:** 1031-1034.
2. Merritts D, Bull WB. Interpreting Quaternary uplift rates at the Mendocino triple junction, northern California, from uplifted marine terraces. *Geology* 1989, **17**(11)**:** 1020-1024.
3. Saillard M, Hall S, Audin L, Farber D, Regard V, Hérail G. Andean coastal uplift and active tectonics in southern Peru: ^{10}Be surface exposure dating of differentially uplifted marine

terrace sequences (San Juan de Marcona,~ 15.4 S). *Geomorphology* 2011, **128**(3-4)**:** 178-190.

4. Matsu'ura T, Komatsubara J, Wu C. Accurate determination of the Pleistocene uplift rate of the NE Japan forearc from the buried MIS 5e marine terrace shoreline angle. *Quat Sci Rev* 2019, **212:** 45-68.
5. Chen Y-G, Liu T-K. Sea level changes in the last several thousand years, Penghu Islands, Taiwan Strait. *Quat Res* 1996, **45**(3)**:** 254-262.
6. Bird MI, Fifield LK, Teh T, Chang C, Shirlaw N, Lambeck K. An inflection in the rate of early mid-Holocene eustatic sea-level rise: A new sea-level curve from Singapore. *Estuarine Coastal Shelf Sci* 2007, **71**(3-4)**:** 523-536.
7. Hanebuth T, Stattegger K, Grootes PM. Rapid flooding of the Sunda Shelf: a late-glacial sea-level record. *Science* 2000, **288**(5468)**:** 1033-1035.
8. Chen W-S, Yang C-Y, Chen S-T, Huang Y-C. New insights into Holocene marine terrace development caused by seismic and aseismic faulting in the Coastal Range, eastern Taiwan. *Quat Sci Rev* 2020, **240:** 106369.
9. Hsieh M-L, Liew P-M, Hsu M-Y. Holocene tectonic uplift on the Hua-tung coast, eastern Taiwan. *Quat Int* 2004, **115-116:** 47-70.
10. Dalca AV, Ferrier KL, Mitrovica JX, Perron JT, Milne GA, Creveling JR. On postglacial sea level–III. Incorporating sediment redistribution. *Geophys J Int* 2013, **194**(1)**:** 45-60.
11. Ferrier KL, Mitrovica JX, Giosan L, Clift PD. Sea-level responses to erosion and deposition of sediment in the Indus River basin and the Arabian Sea. *Earth Planet Sci Lett* 2015, **416:** 12-20.
12. Dadson SJ, Hovius N, Chen H, Dade WB, Hsieh M-L, Willett SD*, et al.* Links between erosion, runoff variability and seismicity in the Taiwan orogen. *Nature* 2003, **426**(6967)**:** 648-651.
13. Derrieux F, Siame LL, Bourlès DL, Chen R-F, Braucher R, Léanni L*, et al.* How fast is the denudation of the Taiwan mountain belt? Perspectives from in situ cosmogenic ^{10}Be. *J Asian Earth Sci* 2014, **88:** 230-245.
14. Liu JP, Liu CS, Xu KH, Milliman JD, Chiu JK, Kao SJ*, et al.* Flux and fate of small mountainous rivers derived sediments into the Taiwan Strait. *Mar Geol* 2008, **256**(1-4)**:** 65-76.
15. Shyu JBH, Sieh K, Chen Y-G, Liu C-S. Neotectonic architecture of Taiwan and its implications for future large earthquakes. *J Geophys Res: Solid Earth* 2005, **110**(B8)**:** B08402.
16. Yu S-B, Chen H-Y, Kuo L-C. Velocity field of GPS stations in the Taiwan area.

Tectonophysics 1997, **274**(1-3)**:** 41-59.

17. Shyu JBH, Sieh K, Chen Y-G. Tandem suturing and disarticulation of the Taiwan orogen revealed by its neotectonic elements. *Earth Planet Sci Lett* 2005, **233**(1-2)**:** 167-177.
18. Chen WS, Wu YM, Yeh PY, Lai YX, Ke SS, Ke MC*, et al.* Insights into the seismogenic structures of the arc-continent convergent plate boundary in eastern Taiwan. *Terr, Oceanic Atmos Sci* 2024, **35:** 13.
19. Shyu JBH, Yin Y-H, Chen C-H, Chuang Y-R, Liu S-C. Updates to the on-land seismogenic structure source database by the Taiwan Earthquake Model (TEM) project for seismic hazard analysis of Taiwan. *Terr, Oceanic Atmos Sci* 2020, **31**(4)**:** 469-478.
20. Shih T-T, Tsai W-T, Hsu M-Y, Mezaki S, Motoharu K. The study of ages and terraces of coral reef in the Kenting National Park area (in Chinese with English abstract): Kenting National Park Administration; 1989.
21. Wang Y, Lin YN, Ota Y, Chung L-H, Shyu JBH, Chiang H-W*, et al.* Mud diapir or fault-related fold? On the development of an active mud-cored anticline offshore southwestern Taiwan. *Tectonics* 2022, **41**(9)**:** e2022TC007234.
22. Farrell WE, Clark JA. On postglacial sea level. *Geophys J Int* 1976, **46**(3)**:** 647-667.
23. Kendall RA, Mitrovica JX, Milne GA. On post-glacial sea level – II. Numerical formulation and comparative results on spherically symmetric models. *Geophys J Int* 2005, **161**(3)**:** 679-706.
24. Ruetenik GA, Ferrier KL, Creveling JR, Fox M. Sea-level responses to rapid sediment erosion and deposition in Taiwan. *Earth Planet Sci Lett* 2020, **538:** 116198.
25. Peltier WR, Argus DF, Drummond R. Space geodesy constrains ice age terminal deglaciation: The global ICE-6G_C (VM5a) model. *J Geophys Res: Solid Earth* 2015, **120**(1)**:** 450-487.
26. Fellin MG, Chen C-Y, Willett SD, Christl M, Chen Y-G. Erosion rates across space and timescales from a multi-proxy study of rivers of eastern Taiwan. *Global Planet Change* 2017, **157:** 174-193.
27. Chen C-Y, Willett SD, Christl M, Shyu JBH. Drainage basin dynamics during the transition from early to mature orogeny in Southern Taiwan. *Earth Planet Sci Lett* 2021, **562:** 116874.
28. Fuller CW, Willett SD, Fisher D, Lu CY. A thermomechanical wedge model of Taiwan constrained by fission-track thermochronometry. *Tectonophysics* 2006, **425**(1-4)**:** 1-24.
29. Willett SD, Fisher D, Fuller C, Yeh E-C, Lu C-Y. Erosion rates and orogenic-wedge kinematics in Taiwan inferred from fission-track thermochronometry. *Geology* 2003, **31**(11)**:** 945-948.

30. Liu C-M, Song S-R, Kuo C-H. Silica geothermometry applications in the Taiwan orogenic belt. *Terr, Oceanic Atmos Sci* 2015, **26**(4)**:** 387-396.
31. Liew PM, Kuo CM, Huang SY, Tseng MH. Vegetation change and terrestrial carbon storage in eastern Asia during the Last Glacial Maximum as indicated by a new pollen record from central Taiwan. *Global Planet Change* 1998, **16-17:** 85-94.
32. Ma T, Tarasov PE, Huang K, Leipe C, Man M, Zheng Z. Intensified climate drying and cooling during the last glacial culmination (20.8–17.5 cal ka BP) in the south-eastern Asian monsoon domain inferred from a high-resolution pollen record. *Quat Sci Rev* 2022, **278:** 107371.
33. Yang T-N, Lee T-Q, Meyers PA, Song S-R, Kao S-J, Löwemark L*, et al.* Variations in monsoonal rainfall over the last 21 kyr inferred from sedimentary organic matter in Tung-Yuan Pond, southern Taiwan. *Quat Sci Rev* 2011, **30**(23-24)**:** 3413-3422.
34. Hsieh M-L, Lai T-H, Wu L-C, Lu W-C, Liu H-T, Liew P-M. Eustatic sea-level change of 11-5 ka in western Taiwan, constrained by radiocarbon dates of core sediments. *Terr, Oceanic Atmos Sci* 2006, **17**(2)**:** 353-370.
35. Huh C-A, Liu JT, Lin H-L, Xu JP. Tidal and flood signatures of settling particles in the Gaoping submarine canyon (SW Taiwan) revealed from radionuclide and flow measurements. *Mar Geol* 2009, **267**(1-2)**:** 8-17.
36. Ujiié Y, Ujiié H, Taira A, Nakamura T, Oguri K. Spatial and temporal variability of surface water in the Kuroshio source region, Pacific Ocean, over the past 21,000 years: evidence from planktonic foraminifera. *Mar Micropaleontol* 2003, **49**(4)**:** 335-364.
37. Hsu H-H, Liu C-S, Chen T-T, Hung H-T. Stratigraphic framework and sediment wave fields associated with canyon-levee systems in the Huatung Basin offshore Taiwan Orogen. *Mar Geol* 2021, **433:** 106408.
38. Yang Y-J. Environment evolution of the western coastal plain in Taiwan since the last glacial maximum period (in Chinese with English abstract). Master thesis, National Taiwan University, Taipei, 2016.
39. Shyu JBH. The sedimentary environment of southern Pingdong Plain since the Last Glacial (in Chinese with English abstract). Master thesis, National Taiwan University, Taipei, 1999.
40. Chang J-H, Hsu H-H, Su C-C, Liu C-S, Hung H-T, Chiu S-D. Tectono-sedimentary control on modern sand deposition on the forebulge of the Western Taiwan Foreland Basin. *Mar Pet Geol* 2015, **66:** 970-977.
41. Boggs S, Wang W-C, Lewis FS, Chen J-C. Sediment properties and water characteristics of

the Taiwan shelf and slope. *Acta Oceanographica Taiwanica* 1979, **10:** 10-49.

42. Dziewonski AM, Anderson DL. Preliminary reference Earth model. *Phys Earth Planet Inter* 1981, **25**(4)**:** 297-356.
43. Lin AT, Watts AB. Origin of the West Taiwan basin by orogenic loading and flexure of a rifted continental margin. *J Geophys Res: Solid Earth* 2002, **107**(B9)**:** 2185.
44. Lu Z, Li C-F, Zhu S, Audet P. Effective elastic thickness over the Chinese mainland and surroundings estimated from a joint inversion of Bouguer admittance and coherence. *Phys Earth Planet Inter* 2020, **301:** 106456.
45. Mao X, Wang Q, Liu S, Xu M, Wang L. Effective elastic thickness and mechanical anisotropy of South China and surrounding regions. *Tectonophysics* 2012, **550-553:** 47-56.
46. Chen B, Chen C, Kaban MK, Du J, Liang Q, Thomas M. Variations of the effective elastic thickness over China and surroundings and their relation to the lithosphere dynamics. *Earth Planet Sci Lett* 2013, **363:** 61-72.
47. Ma K-F, Song T-RA. Thermo-mechanical structure beneath the young orogenic belt of Taiwan. *Tectonophysics* 2004, **388**(1-4)**:** 21-31.
48. Creveling JR, Mitrovica JX, Hay CC, Austermann J, Kopp RE. Revisiting tectonic corrections applied to Pleistocene sea-level highstands. *Quat Sci Rev* 2015, **111:** 72-80.
49. Dutton A, Lambeck K. Ice volume and sea level during the last interglacial. *Science* 2012, **337**(6091)**:** 216-219.
50. Simms AR, Lambeck K, Purcell A, Anderson JB, Rodriguez AB. Sea-level history of the Gulf of Mexico since the Last Glacial Maximum with implications for the melting history of the Laurentide Ice Sheet. *Quat Sci Rev* 2007, **26**(7)**:** 920-940.
51. Jungdal-Olesen G, Pedersen VK, Andersen JL, Gomez N, Mitrovica JX. Sea level response to late Pliocene-Quaternary erosion and deposition in Scandinavia. *Quat Sci Rev* 2023, **301:** 107938.
52. Teng LS. Extensional collapse of the northern Taiwan mountain belt. *Geology* 1996, **24**(10)**:** 949-952.
53. Tsai J-Y. Marine terraces and their neotectonic implications along the northeastern coast of Taiwan (in Chinese with English abstract). Master thesis, National Taiwan Normal University, Taipei, 2013.
54. Hsiao P-T, Hu C-C, Lin K-A, Hsu S-H, Fuh S-C, Chang T-Y*, et al.* Hydrocarbon potential evaluation of Penghu Basin (in Chinese with English abstract). *Petroleum Geology of Taiwan* 1991, **26:** 215-229.

55. Yuan Y-W. Active deformation of coastal and fluvial terraces by the blind Miaoli frontal structure in the Miaoli coastal area, western Taiwan (in Chinese with English abstract). Master thesis, National Taiwan University, Taipei, 2018.
56. Shyu JBH, Sieh K, Avouac JP, Chen W-S, Chen Y-G. Millennial slip rate of the Longitudinal Valley fault from river terraces: Implications for convergence across the active suture of eastern Taiwan. *J Geophys Res: Solid Earth* 2006, **111**(B8)**:** B08403.
57. Huang W-J, Johnson KM, Fukuda Ji, Yu S-B. Insights into active tectonics of eastern Taiwan from analyses of geodetic and geologic data. *J Geophys Res: Solid Earth* 2010, **115:** B03413.
58. Austermann J, Mitrovica JX, Latychev K, Milne GA. Barbados-based estimate of ice volume at Last Glacial Maximum affected by subducted plate. *Nat Geosci* 2013, **6**(7)**:** 553-557.
59. Latychev K, Mitrovica JX, Tromp J, Tamisiea ME, Komatitsch D, Christara CC. Glacial isostatic adjustment on 3-D Earth models: a finite-volume formulation. *Geophys J Int* 2005, **161**(2)**:** 421-444.
60. Crawford O, Al-Attar D, Tromp J, Mitrovica JX, Austermann J, Lau HCP. Quantifying the sensitivity of post-glacial sea level change to laterally varying viscosity. *Geophys J Int* 2018, **214**(2)**:** 1324-1363.
61. Gomez N, Latychev K, Pollard D. A coupled ice sheet-sea level model incorporating 3D Earth structure: Variations in Antarctica during the last deglacial retreat. *J Clim* 2018, **31**(10)**:** 4041-4054.
62. Krien Y, Karpytchev M, Ballu V, Becker M, Grall C, Goodbred S*, et al.* Present-Day Subsidence in the Ganges-Brahmaputra-Meghna Delta: Eastern Amplification of the Holocene Sediment Loading Contribution. *Geophys Res Lett* 2019, **46**(19)**:** 10764-10772.
63. Kirby E, Whipple KX. Expression of active tectonics in erosional landscapes. *J Struct Geol* 2012, **44:** 54-75.
64. Walling DE, Webb BW. Erosion and sediment yield: a global overview. *IAHS Publications* 1996, **236:** 3-20.
65. Burov EB, Diament M. The effective elastic thickness (Te) of continental lithosphere: What does it really mean? *J Geophys Res: Solid Earth* 1995, **100**(B3)**:** 3905-3927.
66. Watts AB, Burov EB. Lithospheric strength and its relationship to the elastic and seismogenic layer thickness. *Earth Planet Sci Lett* 2003, **213**(1-2)**:** 113-131.
67. Ferrier KL, Austermann J, Mitrovica JX, Pico T. Incorporating sediment compaction into a gravitationally self-consistent model for ice age sea-level change. *Geophys J Int* 2017, **211**(1)**:** 663-672.

68. Peltier WR. The impulse response of a Maxwell Earth. *Rev Geophys* 1974, **12**(4)**:** 649-669.
69. Kuchar J, Milne G, Wolstencroft M, Love R, Tarasov L, Hijma M. The influence of sediment isostatic adjustment on sea level change and land motion along the U.S. Gulf Coast. *J Geophys Res: Solid Earth* 2018, **123**(1)**:** 780-796.
70. Argus DF, Peltier WR, Drummond R, Moore AW. The Antarctica component of postglacial rebound model ICE-6G_C (VM5a) based on GPS positioning, exposure age dating of ice thicknesses, and relative sea level histories. *Geophys J Int* 2014, **198**(1)**:** 537-563.
71. Peltier WR. Global glacial isostasy and the surface of the ice-age Earth: The ICE-5G (VM2) model and GRACE. *Annu Rev Earth Planet Sci* 2004, **32**(1)**:** 111-149.
72. Waelbroeck C, Labeyrie L, Michel E, Duplessy JC, McManus JF, Lambeck K*, et al.* Sea-level and deep water temperature changes derived from benthic foraminifera isotopic records. *Quat Sci Rev* 2002, **21**(1)**:** 295-305.
73. Dyer B, Austermann J, D'Andrea WJ, Creel RC, Sandstrom MR, Cashman M*, et al.* Sea-level trends across The Bahamas constrain peak last interglacial ice melt. *Proc Natl Acad Sci USA* 2021, **118**(33)**:** e2026839118.
74. Austermann J, Mitrovica JX. Calculating gravitationally self-consistent sea level changes driven by dynamic topography. *Geophys J Int* 2015, **203**(3)**:** 1909-1922.
75. Mitrovica JX, Milne GA. On the origin of late Holocene sea-level highstands within equatorial ocean basins. *Quat Sci Rev* 2002, **21**(20-22)**:** 2179-2190.
76. Simms AR, Anderson JB, DeWitt R, Lambeck K, Purcell A. Quantifying rates of coastal subsidence since the last interglacial and the role of sediment loading. *Global Planet Change* 2013, **111:** 296-308.

Fig. 1 SIA and its significance. a, Erosional unloading causes crustal uplift and relative sea-level fall, while depositional loading causes crustal subsidence and relative sea-level rise. **b**, We consider a coast that has been uplifted by an active reverse fault (the red curve line). In Case A, the coast has been uplifted due to SIA (ΔR_{up}), making the tectonic uplift (ΔR_{tec}) smaller than the observed crustal uplift (ΔR_{ob}) that did not account for SIA effects, which is determined by taking the height difference between paleo-shoreline angle and the paleo-sea surface. Conversely, in case B, where the coast experienced subsidence due to SIA (ΔR_{sub}), the actual tectonic uplift (ΔR_{tec}) would exceed the observed value (ΔR_{ob}).

Fig. 2 Geological setting and reconstructed sediment transfer scenario of Taiwan. a,

Topography, bathymetry, and tectonic framework of Taiwan [17]. DF: Deformation front; LVS: Longitudinal Valley suture; CMR: Central Mountain Range; CP: coastal plain areas; PB: Puli Basin. **b**, The sea-level history of the Taiwan Strait driven by global ice volume change [25] that enabled us to divide the simulated period into five time intervals, each with distinct deposition rates and patterns. The line at 15 ka marks when post-LGM sediments on the coastal plains started to deposit on the sequence boundary, and the line at 14 ka indicates the timing of Taiwan Strait's inundation. **c-d**, Reconstructed erosion and deposition rate maps of the highstand and lowstand intervals. Erosion rates remain constant through time while deposition patterns vary due to sea-level fluctuation (see text). The deposition pattern of the transition period between highstands and lowstands is shown in **Supplementary Figure S9**.

Fig. 3 Sea-level change due to SIA since 122 kyr. a-f, Cumulative changes of calculated sea-level change (ΔSL_{GR}, defined by $\Delta G - \Delta R$, **a, d**), crustal elevation (**b, e**), and sea surface equipotential (**c, f**) since 122 ka. As mentioned in the Methods, note that ΔSL_{GR} only applies to places where changes in ice thickness and sediment thickness are negligible (e.g., uneroded paleoshorelines). Panels **a–c** and **d–f** are outputs from simulations that used the LT10 and LT30 Earth models, respectively, using the same input ice and sediment models. Numbered sites in **a** are the selected coasts in **g–l**. **g–l**, Relative sea-level curves in simulations that account for SIA effects (red and orange solid curves, with uncertainties modeled by adjusting erosion and deposition rates by 10% faster or slower in the sediment transfer history, corresponding to averaged uncertainties in the rates used) and simulations that neglect SIA effects (blue and purple dashed curves, many of them are overlapping) at the northwestern coast (**g**), northeastern coast (**h**), central eastern coast (**i**), Penghu (**j**), Liuchiu Island (**k**), and Hengchun (**l**). Red and blue curves are results of LT10 Earth model, and orange and purple curves are results of LT30. Darker colored curve in each panel represents the more appropriate result for that coast.

Fig. 4 Simulations neglecting SIA and difference between simulations with and without accounting SIA. We ran another two simulations that are driven only by the ICE-6G ice history and do not account for SIA, one with the LT10 Earth model (**a–c**) and the other with the LT30 Earth model (**d–f**). Panels **a–f** show the contribution of global ice and sea water volume change and the effects of GIA. The short wavelength changes of crustal elevation and sea-level is due to the changes in water load in the ocean but not on land, as well as the thin elastic lithosphere in the adopted Earth models [75]. The differences in each quantity between the simulations that account for

SIA and those neglect it are shown in panel **g–l**, which are the differences between panels **a–f** in Fig. 3 and those in this figure. Panels **g–l** demonstrate the net effect of SIA in our simulations. As in Fig. 3, this figure also shows the cumulative changes over 122 kyr of sea-level change (**a, d, g, j**), crustal elevation (**b, e, h, k**), and sea surface equipotential (**c, f, i, l**).

Fig. 5 Comparison between modeled and observed sea-level histories and re-examination of coastal tectonic uplift rates. (a) Dated marine terraces of Taiwan (blue and purple lines) with the locations of selected coasts in **b–g**. Active reverse and normal faults are marked in red and orange lines, respectively. **b–c**, Comparison between dated sea-level markers (green) and modeled sea-level curves in tectonically stable areas. Symbol of curves are same as Fig. **3g–l**. The widths and heights of the green markers show the uncertainty in age and elevation of the sea-level markers. **d–g**, Utilizing sea-level curves accounting for SIA effects to assess the actual tectonic uplifts at each coast. Results for site α, β, and γ in Fig. 5a are shown in **Supplementary Figure S10**. **h**, Calculated tectonic rock uplift rates that account for SIA (red and orange) versus those do not (blue and purple) and the errors associated with neglecting SIA in percentage (red and orange bars and crosses) at each site.

Table 1. Reported effects of SIA on sea-level change along the coasts of different regions.

Studies	Largest sea-level changes related to SIA along the coast (m)		Region
	Since mid-Holocene	Since Last Interglacial	
Simms et al., 2013 [76]	–	~10 m (rise)	East Texas
Dalca et al., 2013 [10]	–	~10 m (rise) *	Mississippi Delta
Kuchar et al., 2018 [69]	~1–2 m (rise)	–	Mississippi Delta
Ferrier et al., 2015 [11]	~4 m (rise)	~15 m (rise)	Indus Delta
Jungdal-Olesen et al., 2023 [51]	–	~50 m (fall) #	Scandinavia
This study	~20 m (fall) ~7 m (rise)	~200 m (fall) ~70 m (rise)	Taiwan

* The study assumed an idealized, instantaneous, and single sediment pulse into the Gulf of Mexico.

[#] The study found SIA-driven sea-level fall of ~50–100 m along the southern coast of Norway over the last two glacial cycles.

Acknowledgements

The authors sincerely thank Yu Wang for insightful discussions, Chia-Hsun Lin for technical support in numerical modeling, and Hoi Ling Birdie Chou for graphical suggestions. We also thank three anonymous reviewers for their constructive comments and suggestions, which significantly improved this article. This research was supported by the National Science and Technology Council (NSTC) of Taiwan (Project 110-2116-M-002-019, 111-2116-M-002-044, 112-2116-M-002-030, and 113-2116-M-002-025-MY2 to JBHS).

Author Contribution

AH contributed to conceptualization, data curation, formal analysis, model implementation, validation, visualization, writing-original draft, and writing-review and editing. JBHS contributed to conceptualization, project administration, funding acquisition, supervision, writing-original draft, and writing-review and editing. ET and KLF contributed to methodology, software, validation, and writing-review and editing.

Competing interests

The authors declare no competing interests.

Editorial summary:

Along Taiwan's coasts, rapid sediment redistribution can drive sea-level changes with large spatial variability, leading to substantial errors in tectonic uplift estimates, according to a numerical sea-level model simulation.

Peer review information:

Communications Earth and Environment thanks the anonymous reviewers for their contribution to the peer review of this work. Primary Handling Editors: Shan Liu and Martina Grecequet. [A peer review file is available.]

Sediment isostatic adjustment

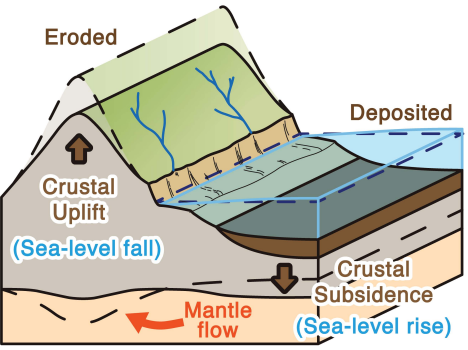

Sea-level responses

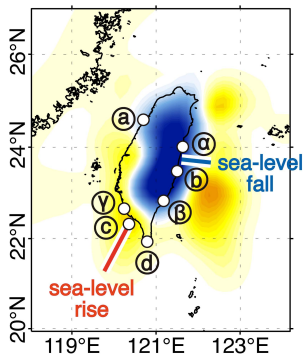

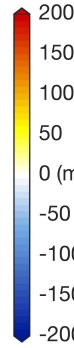

Isostatic responses

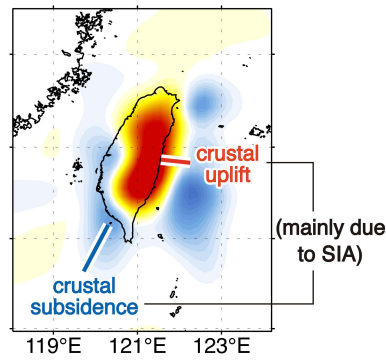

Resiving tectonic coastal uplift estimates

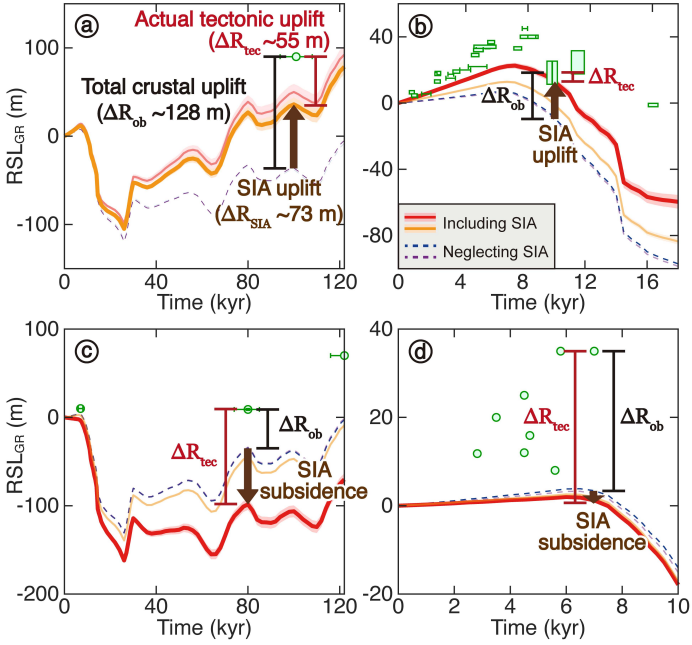

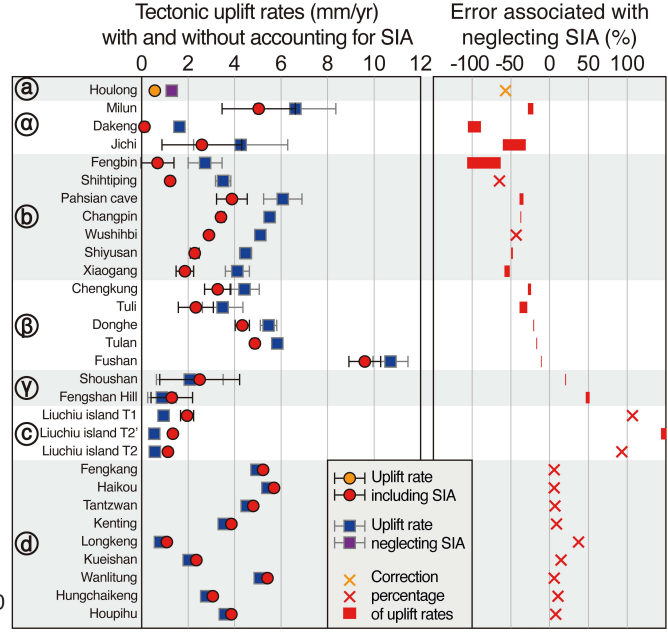

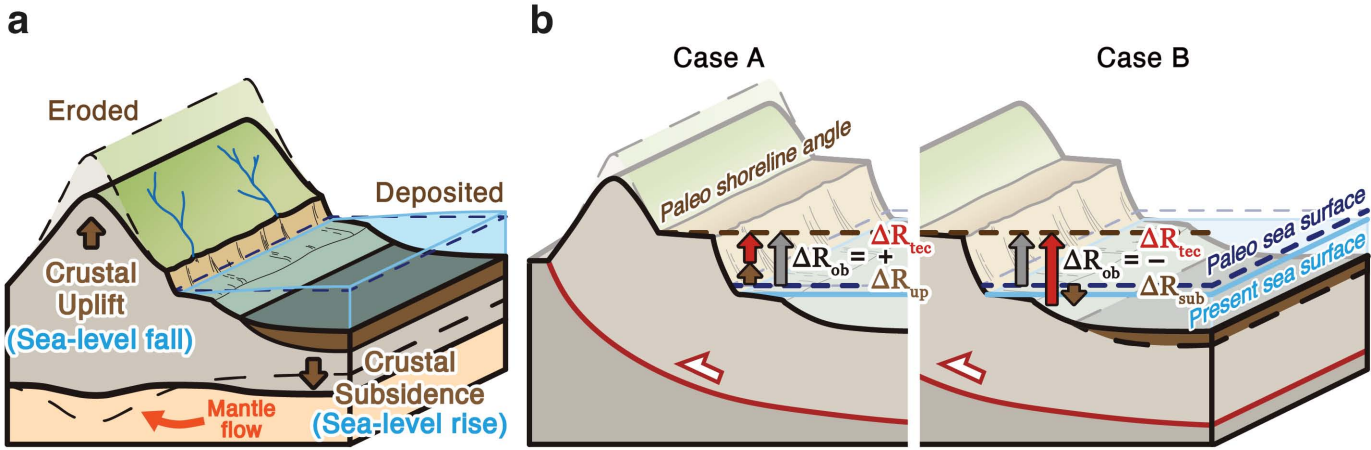
a
Eroded
Deposited
Crustal
Uplift
(Sea-level fall)
Crustal
Subsidence
(Sea-level rise)
Mantle
flow
b
Case A
Case B
Paleo shoreline angle
ΔR_ob = + ΔR_tec ΔR_up
ΔR_ob = − ΔR_tec ΔR_sub
Paleo sea surface
Present sea surface

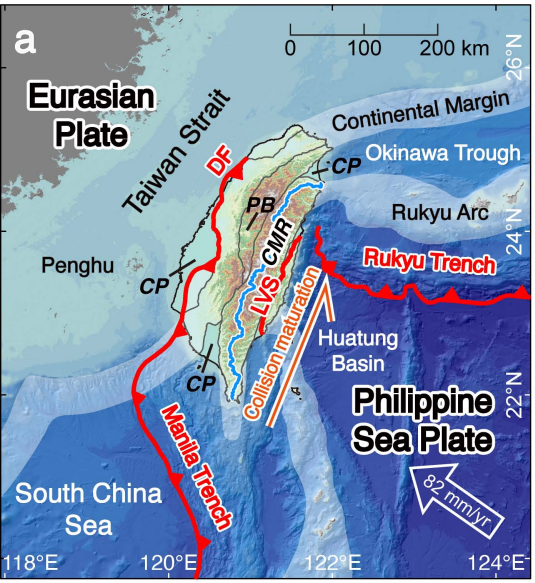
a
0 100 200 km
Eurasian Plate
Taiwan Strait
Continental Margin
Okinawa Trough
DF
CP
PB
Rukyu Arc
CMR
LVS
Penghu
CP
Rukyu Trench
Collision maturation
Huatung Basin
CP
Philippine Sea Plate
Manila Trench
South China Sea
82 mm/yr
26°N
24°N
22°N
118°E
120°E
122°E
124°E

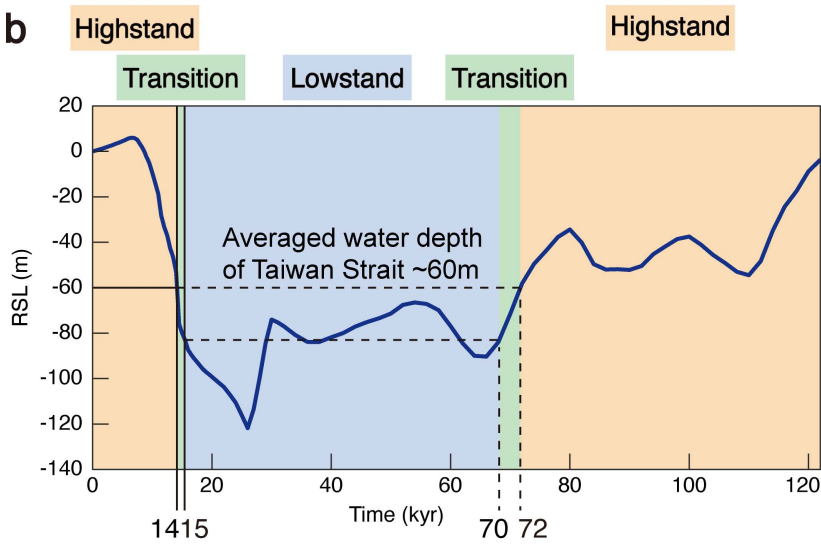
b
Highstand
Transition
Lowstand
Transition
Highstand
Averaged water depth of Taiwan Strait ~60m
RSL (m)
20
0
-20
-40
-60
-80
-100
-120
-140
0
20
40
60
80
100
120
Time (kyr)
1415
70
72

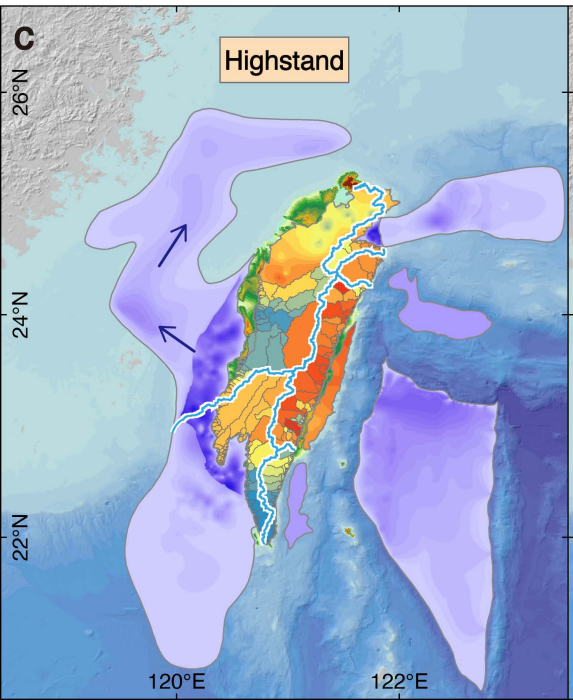
c
Highstand
26°N
24°N
22°N
120°E
122°E

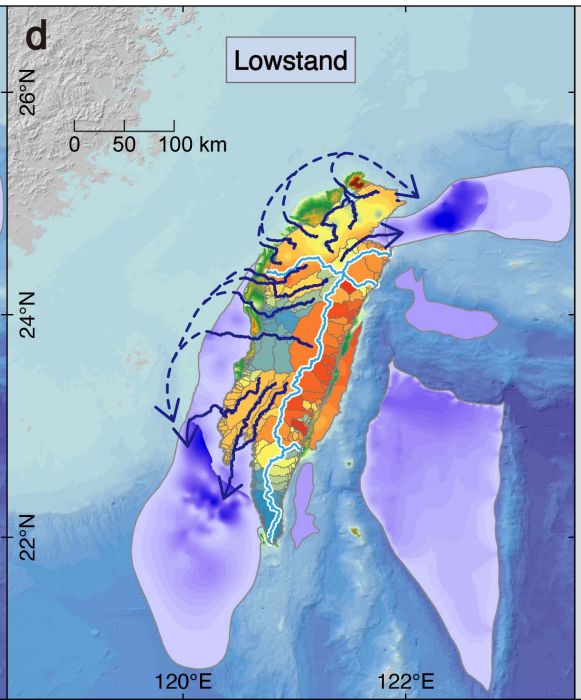
d
Lowstand
0 50 100 km
26°N
24°N
22°N
120°E
122°E

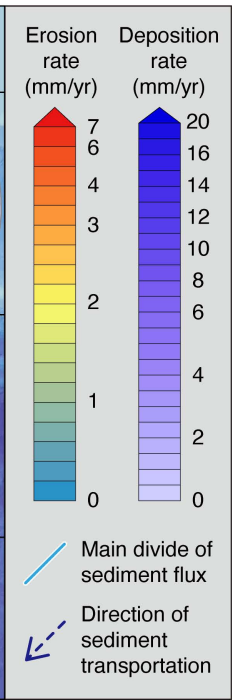
Erosion rate (mm/yr)
7
6
4
3
2
1
0
Deposition rate (mm/yr)
20
16
14
12
10
8
6
4
2
0
Main divide of sediment flux
Direction of sediment transportation

$\Delta SL_{GR} = - \Delta R + \Delta G$

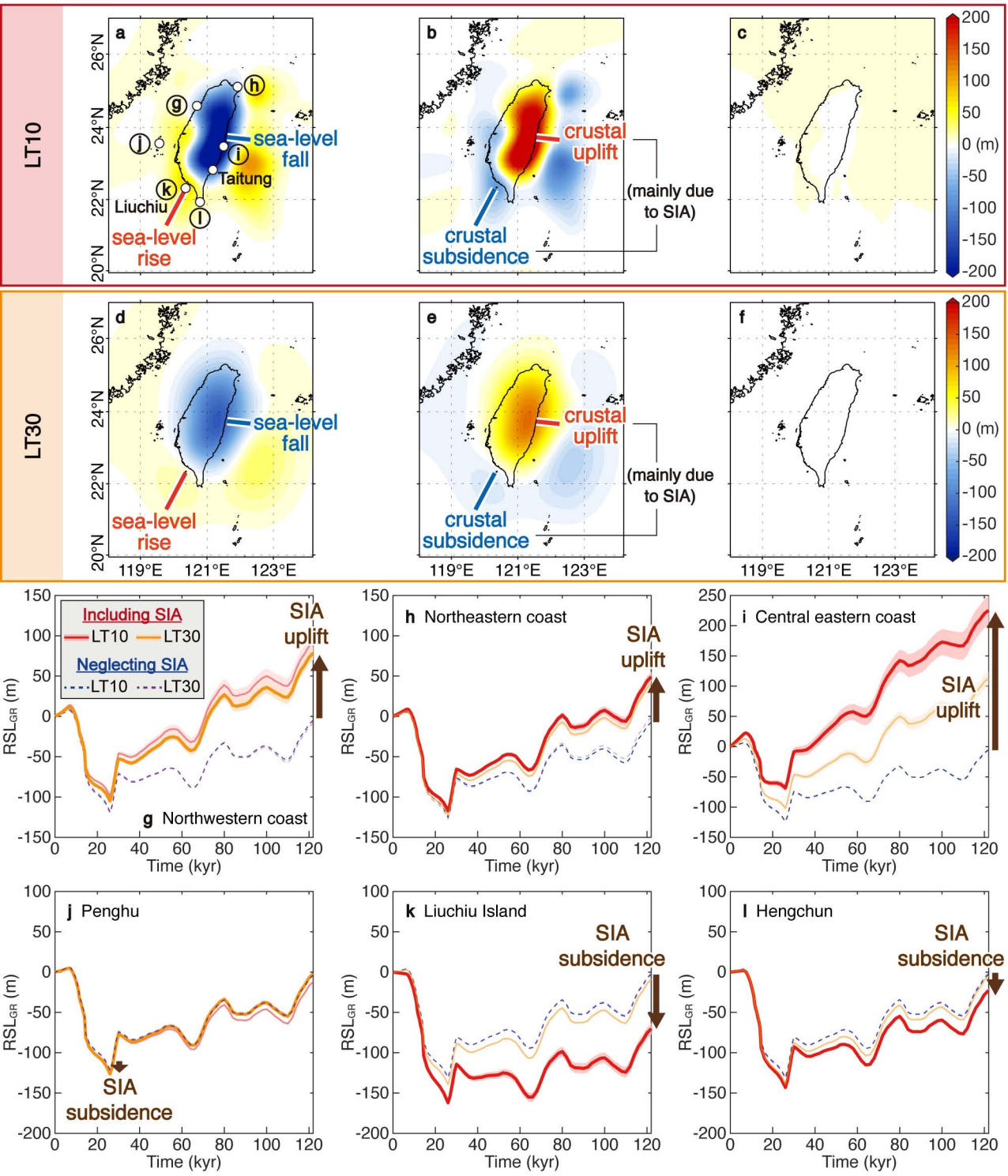

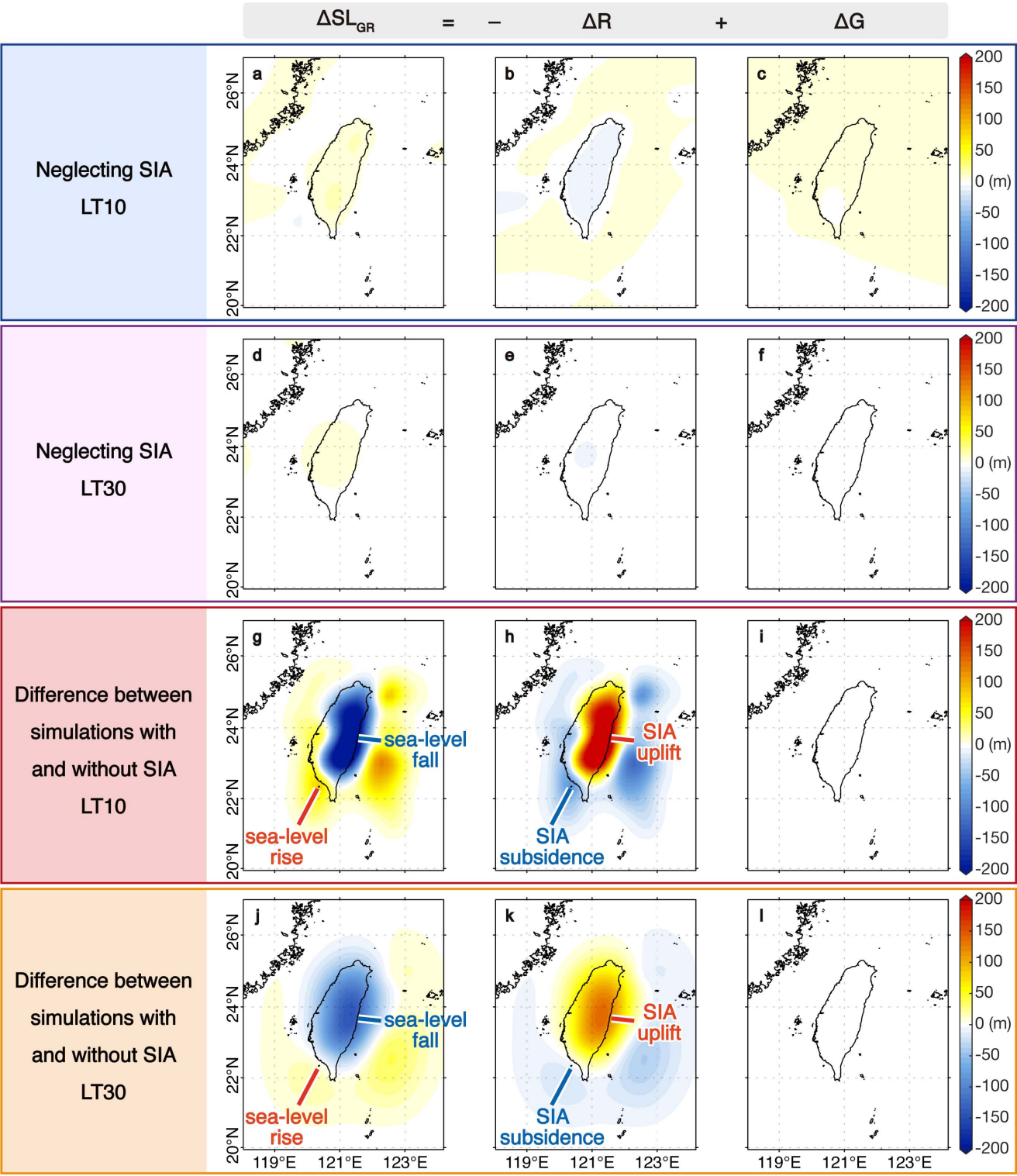
ΔSL_GR = − ΔR + ΔG
Neglecting SIA
LT10
Neglecting SIA
LT30
Difference between
simulations with
and without SIA
LT10
Difference between
simulations with
and without SIA
LT30
a
b
c
d
e
f
g
h
i
j
k
l
sea-level
fall
sea-level
rise
SIA
uplift
SIA
subsidence
20°N
22°N
24°N
26°N
119°E
121°E
123°E
200
150
100
50
0 (m)
-50
-100
-150
-200

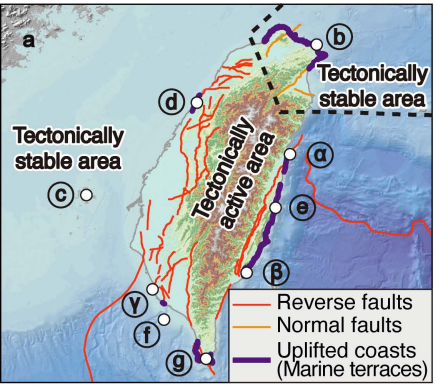

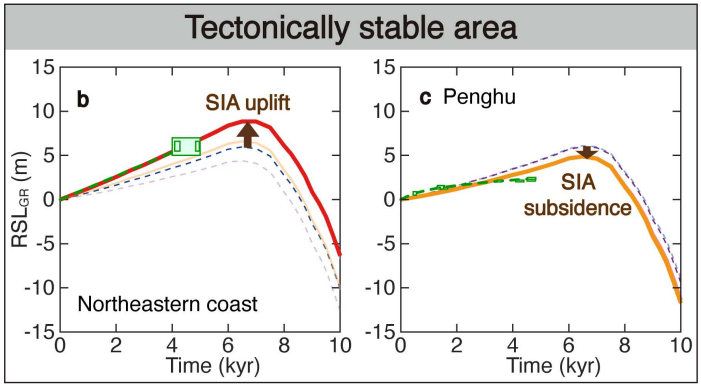

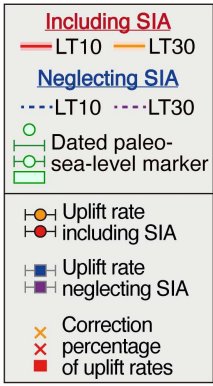

Tectonically active area